

Exact projected entangled pair ground states with topological Euler invariant

Thorsten B. Wahl,^{1,*} Wojciech J. Jankowski,¹ Adrien Bouhon,^{1,2} Gaurav Chaudhary,¹ and Robert-Jan Slager^{1,†}

¹*TCM Group, Cavendish Laboratory, Department of Physics,
J J Thomson Avenue, Cambridge CB3 0HE, United Kingdom*

²*Nordita, Stockholm University and KTH Royal Institute of Technology,
Hannes Alfvéns väg 12, SE-106 91 Stockholm, Sweden*

(Dated: July 19, 2024)

We report on a class of gapped projected entangled pair states (PEPS) with non-trivial Euler topology motivated by recent progress in band geometry. In the non-interacting limit, these systems have optimal conditions relating to saturation of quantum geometrical bounds, allowing for parent Hamiltonians whose lowest bands are completely flat and which have the PEPS as unique ground states. Protected by crystalline symmetries, these states evade restrictions on capturing tenfold-way topological features with gapped PEPS. These PEPS thus form the first tensor network representative of a non-interacting, gapped two-dimensional topological phase, similar to the Kitaev chain in one dimension. Using unitary circuits, we then formulate interacting variants of these PEPS and corresponding gapped parent Hamiltonians. We reveal characteristic entanglement features shared between the free-fermionic and interacting states with Euler topology. Our results hence provide a rich platform of PEPS models that have, unexpectedly, a finite topological invariant, providing a platform for new spin liquids, quantum Hall physics, and quantum information pursuits.

Introduction.— Tensor network states (TNS) form a generally applicable tool for the description of quantum matter. A numerically efficient representation of the ground states of local gapped Hamiltonians [1–5], TNS play a pivotal role both in the simulation of correlated systems [6–11] and the analytical classification of topological phases [12–17]. Yet, due to the increased complexity in higher dimensions, TNS have not yet matched the success of non-interacting band theory [18, 19], both in simulations and the classification of topological phases [20–26]. Of particular interest are therefore systems which can be well captured with band theory but are marked by difficulties when it comes to TNS approaches. The most well-known such example is chiral topological systems: In topological band theory, they are characterized by occupied bands whose overall Chern number is non-vanishing, separated by a gap from the conduction bands. While TNS approaches are able to capture the chiral topological features of such systems, this comes at the cost of producing algebraically decaying correlations characteristic of critical systems [27–29]. Generally, it has been shown that TNS with exponentially decaying correlations cannot capture any higher-dimensional topological invariant [30] of the ten Altland-Zirnbauer (AZ) classes [31].

The severe restrictions of TNS to represent gapped non-interacting topological phases suggest that TNS might equally struggle to capture topological phases protected by crystalline symmetries. However, reinvigorated interests [32, 33] in relation to quantum geometry [34, 35] could provide a useful tool in that they outline flatband conditions. Under such conditions, it is possible to define topological flatband Hamiltonians that can be formulated as exemplary parent Hamiltonians. These are sums of projectors with local support that each annihi-

late the ground state(s). From these local projectors, a TNS ground state can in principle be constructed. However, whether the resulting state is non-vanishing and can be made the unique ground state of such a crystalline symmetry-protected topological Hamiltonian might be hampered by the previously mentioned hurdles. Intuitively, TNS with exponentially decaying correlations are incompatible with topological invariants, as they come with delocalized edge modes around a physical boundary (in more than one dimension); the local structure of tensor networks is incapable of separating such edge modes from the bulk modes, delocalizing them as well. Because of that, in the following, we consider crystalline symmetry-protected topological phases which do not have helical or chiral edge modes.

We show that a family of topological projected entangled pair states (PEPS) [36] and generating Hamiltonians can be formulated in the context of the Euler class [25, 37–39]. The Euler class is a multi-gap invariant [25], pertaining to topological structures that emerge when groups of partitioned bands (band subspaces) carry non-trivial topological indices [25]. These topological charges of groups of bands can be altered by braiding nodes in momentum space, as band nodes residing between neighboring bands can carry non-Abelian charges [37, 38, 40]. The braiding of non-Abelian frame charges and multi-gap topologies have been increasingly related, both theoretically and experimentally, to physical systems that range from out-of-equilibrium settings [41–43] and phonon spectra [44, 45], to electronic systems (twisted, magnetic and conventional) [38, 46, 47] as well as metamaterials [48–50].

The here introduced family of PEPS has non-trivial Euler class, evading no-go conditions as for tenfold-way topologies [31], constituting a 2D analogue of the Kitaev

chain [51]. Within the non-interacting limit, from a band theory perspective, these PEPS enjoy ideal quantum geometrical properties. More importantly, by applying shallow quantum circuits of diagonal unitaries, we transform these PEPS and their gapped parent Hamiltonians to interacting variants. We can signify the Euler phase both in the non-interacting and the interacting limit upon appealing to the entanglement spectrum. As such, our results set a benchmark for an exact class of PEPS parent Hamiltonians with *finite topological invariant*.

Euler class.— A pair of isolated (gapped from the rest of the spectrum) bands $|u_n(\mathbf{k})\rangle, |u_{n+1}(\mathbf{k})\rangle$ can acquire a non-trivial Euler class χ when it is part of at least a three-band system that enjoys a reality condition assured by the presence of $\mathcal{C}_2\mathcal{T}$ [twofold rotations combined with time-reversal symmetry (TRS)], or \mathcal{PT} symmetry, involving parity and TRS. The Euler class is then concretely obtained as [37, 38]

$$\chi = \frac{1}{2\pi} \int_{\text{BZ}} \text{Eu } dk_1 \wedge dk_2 \in \mathbb{Z}, \quad (1)$$

where one integrates the Euler curvature $\text{Eu} = \langle \partial_{k_1} u_n(\mathbf{k}) | \partial_{k_2} u_{n+1}(\mathbf{k}) \rangle - \langle \partial_{k_2} u_n(\mathbf{k}) | \partial_{k_1} u_{n+1}(\mathbf{k}) \rangle$ over the Brillouin zone (BZ). The pair of bands can either be degenerate (and flat) or feature a number of 2χ nodal points that cannot be annihilated due to the topological nature [25, 37, 38]. Eq. (1) shows that the Euler class is the real analogue of the Chern number. Similarly, the isolated two-band subspace does not admit exponentially-localized Wannier functions in a $\mathcal{C}_2\mathcal{T}$ -symmetric gauge, but unlike the Chern case, the system does not feature protected chiral or helical edge states, allowing for a PEPS representation.

The model.— To concretize the discussion, we consider spinless fermions hopping on the kagome lattice with nearest-neighbor hopping $t = -1$, next-nearest-neighbor

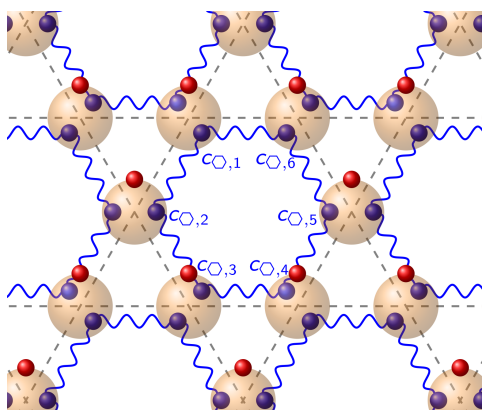


FIG. 1. Projected entangled simplex state. The blue wiggly lines denote the initial state of virtual fermions (blue balls) entangled across hexagons. The transparent red balls denote the projection onto the physical fermions (red balls).

hopping $t' = -1$ and third-nearest-neighbor hopping $t'' = -1$ inside the hexagons. For chemical potential μ , the Hamiltonian thus reads

$$H = \sum_{\langle i,j \rangle} a_i^\dagger a_j + \sum_{\langle\langle i,j \rangle\rangle} a_i^\dagger a_j + \sum_{\langle\langle\langle i,j \rangle\rangle\rangle_{\square}} a_i^\dagger a_j - \mu \sum_{i=1}^N a_i^\dagger a_i, \quad (2)$$

where $\langle i,j \rangle$, $\langle\langle i,j \rangle\rangle$ correspond to nearest- and next-nearest neighbor pairs of sites i, j and $\langle\langle\langle i,j \rangle\rangle\rangle_{\square}$ to third-nearest neighbor pairs of the same hexagons. a_i^\dagger (a_i) are the fermionic creation (annihilation) operators and N the number of sites. The Hamiltonian has two degenerate flat bands at $E = -2 - \mu$ and a dispersive band on top, separated by an energy gap $\Delta = 3$. The flat bands have Euler number $\chi = 1$, protected by $\mathcal{C}_2\mathcal{T}$ symmetry. At $\mu = -2$, both flat bands are at $E = 0$, and the ground states $|\psi_n\rangle$, $n = 0, 1, \dots, 2N/3$ are macroscopically degenerate, characterized by fillings $[0, 1, 2, \dots, 2N/3]$. We now construct the ground state with the highest filling, which will become the unique ground state for $-2 < \mu < 1$. To that end, we note that the Hamiltonian for $\mu = -2$ can be rewritten as

$$H_p = \sum_{\square} \sum_{i,j \in \square} a_i^\dagger a_j = 6 \sum_{\square} a_{\square}^\dagger a_{\square} = 6 \sum_{\square} h_{\square}, \quad (3)$$

where \square denotes the hexagons of the kagome lattice, and we defined $a_{\square} = \frac{1}{\sqrt{6}} \sum_{i \in \square} a_i$ and $h_{\square} = a_{\square}^\dagger a_{\square}$. Hence, the ground states fulfill $a_{\square} |\psi_n\rangle = 0$ for all hexagons \square . The ground state with the highest occupation number is

$$|\psi_{2N/3}\rangle = \prod_{\square} a_{\square} |1 \dots 1\rangle, \quad (4)$$

where $|1 \dots 1\rangle$ is the fully occupied state. Due to $\{a_{\square}, a_{\square'}\} = 0$, the ordering in Eq. (4) is irrelevant. However, notably, for the other commutation relations, we have $\{a_{\square}, a_{\square'}^\dagger\} = \delta_{\square, \square'} + \frac{1}{6} \delta_{\langle \square, \square' \rangle}$, where $\langle \square, \square' \rangle$ denotes corner-sharing, neighboring hexagonal plaquettes. This anticommutation algebra shows that, while the operators a_{\square}^\dagger effectively create fermions in a superposition of six atomic orbitals, the Hamiltonian Eq. (3) is not adiabatically connected to a Hamiltonian of an atomic insulator, despite the functional similarity to such Hamiltonians: In particular, that is the case due to the corner-sharing obstruction, the presence of which is also crucial for the entanglement of the system, as we demonstrate below.

$|\psi_{2N/3}\rangle$ can be written as a projected entangled simplex state (PESS) [52] as follows: We start out with a virtual state of $2N$ spinless fermions – two assigned to each physical fermion. The virtual fermions are in the state $|\omega_v\rangle = \frac{1}{\sqrt{6}} \prod_{\square} \sum_{i=1}^6 c_{\square, i} |1_v\rangle$, where $|1_v\rangle$ denotes the fully occupied virtual state. $c_{\square, i}$ corresponds to virtual fermion $i = 1, \dots, 6$ within hexagon \square (as opposed to the physical particles a_j , there are now unique assignments within hexagons), cf. Fig. 1. The next step

is to map each pair of virtual fermions around a site to one physical fermion. To that end, we use the operator $\hat{M}_j = a_j^\dagger c_j' c_j + c_j' - c_j$. Here, c_j' corresponds to the virtual fermion located on the left of the site j and c_j to the virtual fermion located on its right. We finally project on the vacuum of virtual particles, obtaining the overall state

$$|\psi_{\text{PEPS}}\rangle = \langle 0_v | \prod_{j=1}^N \hat{M}_j \prod_{\square} \frac{1}{\sqrt{6}} \sum_{i=1}^6 c_{\square, i} |1_v 0_p\rangle, \quad (5)$$

where $|1_v 0_p\rangle$ corresponds to the vacuum of physical fermions and fully occupied virtual fermionic state. We already labeled the overall state as a ‘‘PEPS’’, since it can also be written as the more familiar projected entangled pair state, as we show further below. In order to demonstrate that $|\psi_{2N/3}\rangle \propto |\psi_{\text{PEPS}}\rangle$, we first verify that $a_{\square} |\psi_{\text{PEPS}}\rangle = 0$ and later that the PEPS has filling $2N/3$. For the first claim, we notice that

$$\begin{aligned} & \langle 0_v | a_j (a_j^\dagger c_j' c_j + c_j' - c_j) [\dots] |1_v 0_p\rangle \\ &= \langle 0_v | (a_j^\dagger c_j' c_j + c_j' - c_j) c_j' [\dots] |1_v 0_p\rangle \\ &= \langle 0_v | (a_j^\dagger c_j' c_j + c_j' - c_j) c_j [\dots] |1_v 0_p\rangle, \end{aligned} \quad (6)$$

where $[\dots]$ denotes a sum of products of operators that do not act on the physical fermion at site j . We thus have

$$\begin{aligned} a_{\square} |\psi_{\text{PEPS}}\rangle &= \pm \frac{1}{6} \langle 0_v | \prod_j (a_j^\dagger c_j' c_j + c_j' - c_j) \sum_{i=1}^6 c_{\square', i} \times \\ &\times \prod_{\square} \sum_{k=1}^6 c_{\square, k} |1_v 0_p\rangle = 0. \end{aligned} \quad (7)$$

Second, we see that the initial state $|1_v 0_p\rangle$ contains $2N$ virtual and no physical fermions. The operator $\prod_{\square} \sum_{k=1}^6 c_{\square, k}$ reduces that to $2N(1 - 1/6) = 5N/3$ fermions. Finally, each operator \hat{M}_j creates one physical fermion less than it annihilates virtual ones, i.e., we are left with $2N/3$ physical fermions in $|\psi_{\text{PEPS}}\rangle$. Hence, $|\psi_{\text{PEPS}}\rangle \propto |\psi_{2N/3}\rangle$, as claimed.

$|\psi_{\text{PEPS}}\rangle$ is a (non-unique) frustration-free ground state of the parent Hamiltonian H_p and the unique ground state of $H = H_p - (\mu + 2) \sum_{i=1}^N a_i^\dagger a_i$ for $-2 < \mu < 1$. This example shows that PEPS can be the unique ground states of local gapped Hamiltonians with non-trivial two-dimensional crystalline topological features, even in the non-interacting limit. This contrasts with the inability of free-fermionic PEPS to capture any higher-dimensional topological labels of the ten-fold classification unless the PEPS have algebraically decaying correlations [27, 28, 31, 53].

The PESS we have considered so far can be converted into a PEPS by realizing that the simplex states are of the form $|011111\rangle + |101111\rangle + \dots + |111110\rangle$, also

known as a W -state [54], which can be written as a non-translationally invariant matrix product state of bond dimension 2 or a translationally invariant one of bond dimension 6. \hat{M} can be represented as a rank-3 tensor M_{ab}^i with $M_{11}^1 = M_{10}^0 = -M_{01}^0 = 1$ and all other elements equal zero. The resulting PEPS tensor has rank 5 and bond dimension 2 or 6, respectively, see Fig. 2. We note that a similar construction in terms of PESS defined on triangles can be used to describe the ground state of the Hamiltonian (2) for nearest-neighbor hopping only, an Euler insulator with one flat bottom band touched by two dispersive bands from above [48, 49].

Free-fermion generalizations. – A straightforward generalization is obtained by modifying the simplex states to a linear combination, $|\tilde{\omega}_v\rangle = \prod_{\square} \sum_{i=1}^6 \beta_i c_{\square, i} |1_v\rangle$ with $\beta_i \in \mathbb{C}$, and keeping \hat{M}_j the same. The new PEPS is annihilated by $\tilde{a}_{\square} = \sum_{i \in \square} \beta_i a_i$, where we set $\sum_{i=1}^6 |\beta_i|^2 = 1$. This corresponds to the new Hamiltonian

$$\tilde{H} = 6 \sum_{\square} \sum_{i, j \in \square} \beta_i^* \beta_j a_i^\dagger a_j - (\mu + 2) \sum_{i=1}^N a_i^\dagger a_i. \quad (8)$$

One can check that $\mathcal{C}_2\mathcal{T}$ symmetry implies $\beta_{i+3}^* = \beta_i$ ($i = 1, 2, 3$) up to an irrelevant overall phase. Whether

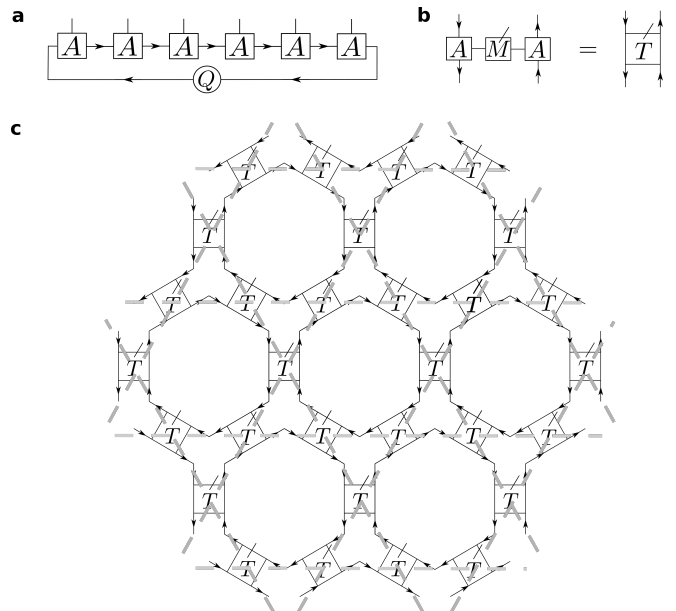


FIG. 2. a: Matrix product state representation of the simplex states residing on the hexagons. A can either be chosen to be of bond dimension $D = 2$, with $A_{12}^0 = 1/\sqrt{6}$, $A_{11}^1 = A_{22}^1 = 1$, $Q_{21} = 1$ and all other elements of A and Q equal to zero, or $D = 6$ with $A_{61}^0 = 1/\sqrt{6}$, $A_{l, l+1}^l = 1$ ($l = 1, \dots, 5$), all other elements of A equal to zero and $Q = \mathbb{1}$ (translationally invariant representation). Incoming arrows denote left and outgoing arrows right lower indices. b: By combining two A tensors with the tensor M , we obtain the tensor T constituting the PEPS. c: PEPS with one rank-5 tensor located on each site of the kagome lattice (gray dashed lines).

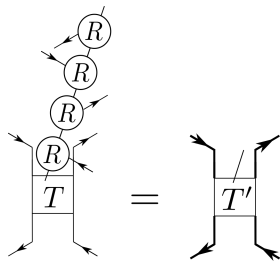


FIG. 3. Construction of the tensors T' forming the building blocks of the interacting $|\psi'_{\text{PEPS}}\rangle$. The R -tensors get absorbed into the T tensor, increasing its bond dimension (indicated by thick directed lines).

this state has a non-zero Euler number depends on the specific choice of the β_i .

Quantum geometry.— We now highlight the ideal quantum geometrical properties due to the flatness of the bottom bands. The flatness is crucial, as it allows for Hamiltonians which are sums of local projectors and therefore have (macroscopically degenerate) ground states at energy $E = 0$. The quantum metric [32–34],

$$g_{ij}^x = \text{Tr}_{\text{occ}}[(\partial_{k_i} \hat{P})(\partial_{k_j} \hat{P})], \quad (9)$$

is defined as a trace over momentum-space projectors $\hat{P} = \sum_{n=1,2} |u_n(\mathbf{k})\rangle \langle u_n(\mathbf{k})|$ of occupied Bloch states $|u_n(\mathbf{k})\rangle$, with the momenta components $k_i, k_j = k_1, k_2$. The flat Euler bands saturate the quantum-geometric bounds due to the Euler invariant χ [33, 55], between the quantum volume elements ($\sqrt{\det \mathbf{g}^x}$) and the Euler curvature ($\sqrt{\det \mathbf{g}^x} = |\text{Eu}|$) across the entire momentum space. Upon integrating, we thus retrieve a quantum volume which is a multiple of 2π ,

$$\text{Vol } \mathbf{g}^x \equiv \oint \sqrt{\det \mathbf{g}^x} dk_1 \wedge dk_2 = 2\pi|\chi|, \quad (10)$$

showcasing the ideal non-Abelian quantum geometry [33, 55]. Upon introducing interactions as below, the many-body quantum metric in the space of twisted boundary conditions can reflect the topological nature of many-body Euler ground states as we also demonstrate in the non-interacting limit [see Supplemental Material (SM) [56]]. Using central relations of quantum metrology [57–59], the ideal condition physically manifests itself through the non-triviality of the quantum Fisher information (QFI). That is, we retrieve a metrological quantum Cramer-Rao (QCR) bound [57] on the realizable model measurements, see SM [56], which could be directly executed in quantum simulators or synthetic three-level systems [60].

Interacting generalizations.— The modified simplex states give rise to non-interacting PEPS. We can further generalize the construction to interacting states by applying a shallow quantum circuit U of diagonal unitaries, which makes it easy to ensure that $\mathcal{C}_2\mathcal{T}$ symmetry

is preserved. Hence, by definition, we remain in the same topological phase. Furthermore, the new state will also be a PEPS of low bond dimension. We consider the simplest case of nearest-neighbor gates. We view these as being applied on all hexagons in a translationally invariant fashion. Within each hexagon, we label $u_{j,j+1}$ as the unitary acting on sites j and $j+1$ ($j = 7 \equiv 1$) inside a given hexagon, with sites enumerated as in Fig. 1. $\mathcal{C}_2\mathcal{T}$ symmetry is achieved if $u_{j,j+1} = u_{j+3,j+4}^*$ for all $j = 1, 2, 3$. The simplest continuously tuneable case is $u_{j,j+1} = \mathbb{1} - (1 - e^{\pm i\alpha})n_j n_{j+1}$ with particle number operators n_j , $\alpha \in [0, 2\pi)$, and positive (negative) sign for $j = 1, 2, 3$ ($j = 4, 5, 6$). The new PEPS is given by $|\psi'_{\text{PEPS}}\rangle = U|\psi_{\text{PEPS}}\rangle$ and the Hamiltonian gets transformed as

$$H' = UH U^\dagger = \sum_{\diamond} \sum_{i,j \in \diamond} a_i^\dagger a_j' - (\mu + 2) \sum_{i=1}^N a_i^\dagger a_i, \quad (11)$$

where we defined $a_i' = U a_i U^\dagger$ and used that U commutes with $n_i = a_i^\dagger a_i$. One can easily verify $a_i'^\dagger = a_i^\dagger \prod_j^{(i,j)} [\mathbb{1} - (1 - e^{i\sigma_{(i,j)}\alpha})n_j]$, where the product runs over all nearest neighbors of site i . $\sigma_{(i,j)} = +1$ if (i,j) corresponds to one of the first three bonds in the hexagon that it lies in and -1 if it corresponds to one of the last three bonds. This gives rise to the overall Hamiltonian

$$H' = \sum_{\diamond} \sum_{i,j \in \diamond} a_i^\dagger \prod_k^{(k,i)} [\mathbb{1} - (1 - e^{i\sigma_{(k,i)}\alpha})n_k] \times \prod_l^{(j,l)} [\mathbb{1} - (1 - e^{-i\sigma_{(j,l)}\alpha})n_l] a_j - (\mu + 2) \sum_{i=1}^N n_i. \quad (12)$$

H' has the same spectrum as H for fixed μ , and $|\psi'_{\text{PEPS}}\rangle$ is therefore its unique ground state for $-2 < \mu < 1$. The Hamiltonian is strictly local, acting on hexagons \diamond and adjacent triangles. This is the first example of an interacting Euler insulator with a local gapped Hamiltonian. $|\psi'_{\text{PEPS}}\rangle$ can be constructed by writing the phase matrix of $u_{j,j+1} = \mathbb{1} - (1 - e^{\pm i\alpha})n_j n_{j+1}$ as $\sum_{q=1}^2 R_q^{ab} R_q^{cd}$ with $R_1^{ab} = \delta_{ab}$ and $R_2^{ab} = \sqrt{-1 + e^{\pm i\alpha}} \delta_{1a} \delta_{1b}$, $a, b \in \{0, 1\}$. (As the underlying operators are even, they can be decomposed into tensor products.) Four nearest-neighbor unitaries act on each site, such that the tensors of $|\psi'_{\text{PEPS}}\rangle$ can be constructed by contracting the physical leg of T with four R -tensors, see Fig. 3. If the bond dimension of T was chosen to be 2, the interacting PEPS has bond dimension $D = 4$.

Entanglement spectra.— We numerically calculated the entanglement spectra of $|\psi'_{\text{PEPS}}\rangle$ for an infinitely long torus with circumference L_y . That is, the torus is bipartitioned with L_y unit cells located around the perimeter of the resulting cylinder. We obtained its entanglement

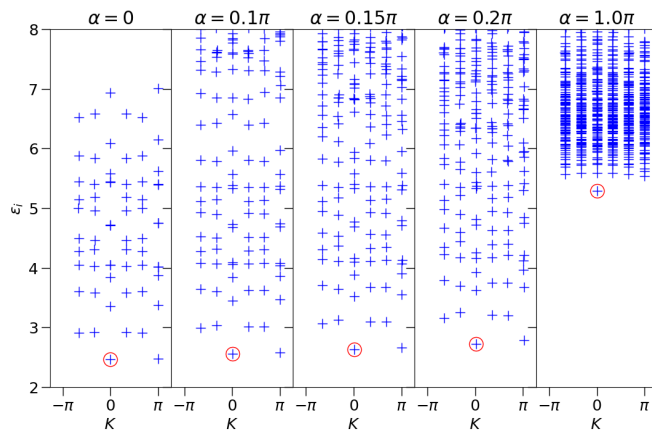


FIG. 4. Entanglement spectra as a function of the many-body momentum K for different values of α for $L_y = 6$. For small values of α , the low-lying spectrum strongly resembles the non-interacting one ($\alpha = 0$). In particular, a cusp at $K = 0$ (highlighted by a red circle) is preserved as α is increased. Parallel to this, new entanglement energies appear at the top of the spectrum and eventually merge with its low-lying part.

spectrum by calculating the non-interacting $|\psi_{\text{PEPS}}\rangle$ using TenPy [61] and applying the quantum circuit U on it to obtain the interacting $|\psi'_{\text{PEPS}}\rangle$. The entanglement spectra for various values of α and $L_y = 6$ are shown in Fig. 4. We observe that the low-lying part of the entanglement spectrum possesses a cusp at momentum $K = 0$, which remains intact as α is increased. This suggests that characteristic features of Euler insulators in the entanglement spectrum are preserved as interactions are turned on. We note that in the more familiar case of Chern insulators, entanglement spectra are qualitatively preserved also only as long as interactions are weak. We further detail the entanglement features of the non-interacting case, including the stable cusp at $K = 0$ in [56].

Discussion and Conclusion. – We leverage quantum geometric conditions to define a class of exact PEPS with finite topological Euler invariant. The enigmatic nature of the Euler class allows to circumvent no-go conditions. Importantly, these models can be generalized to interacting variants and have definite entanglement signatures. As such, these PEPS set a benchmark for new pursuits. These potential pursuits involve studying exotic excitations and spin liquids realized from Euler many-body PEPS ground states. In particular, on introducing interactions, novel kinds of fractionalizations should emerge from the interplay of the many-body entanglement as well as emergent quantum anomalous Hall states [62]. In addition, as all our states can be created by shallow quantum circuits from product states and have topological features, they are also particularly interesting for implementations on noisy intermediate-scale quantum devices and the development of new quantum error correction protocols. We will report on this in the near future.

ACKNOWLEDGMENTS

R.-J. S., G. C. and T. B. W. acknowledge funding from a New Investigator Award, EPSRC grant EP/W00187X/1, a EPSRC ERC underwrite grant EP/X025829/1, and a Royal Society exchange grant IES/R1/221060 as well as Trinity College, Cambridge. W. J. J. acknowledges funding from the Rod Smallwood Studentship at Trinity College, Cambridge.

* tw344@cam.ac.uk

† rjs269@cam.ac.uk

- [1] F. Verstraete and J. I. Cirac, Matrix product states represent ground states faithfully, *Phys. Rev. B* **73**, 094423 (2006).
- [2] Y. Huang, Area law in one dimension: Degenerate ground states and Renyi entanglement entropy, [arXiv:1403.0327](https://arxiv.org/abs/1403.0327) (2014).
- [3] A. Molnar, N. Schuch, F. Verstraete, and J. I. Cirac, Approximating Gibbs states of local Hamiltonians efficiently with projected entangled pair states, *Physical Review B* **91**, 045138 (2015).
- [4] A. M. Dalzell and F. G. S. L. Brandão, Locally accurate MPS approximations for ground states of one-dimensional gapped local Hamiltonians, *Quantum* **3**, 187 (2019).
- [5] Y. Huang, Approximating local properties by tensor network states with constant bond dimension, [arXiv:1903.10048](https://arxiv.org/abs/1903.10048) (2019).
- [6] S. R. White and D. J. Scalapino, Density Matrix Renormalization Group Study of the Striped Phase in the 2D $t - J$ Model, *Phys. Rev. Lett.* **80**, 1272 (1998).
- [7] S. Yan, D. A. Huse, and S. R. White, Spin-Liquid Ground State of the $S = 1/2$ Kagome Heisenberg Antiferromagnet, *Science* **332**, 1201080 (2011).
- [8] P. Corboz and F. Mila, Tensor network study of the Shastry-Sutherland model in zero magnetic field, *Phys. Rev. B* **87**, 115144 (2013).
- [9] P. Corboz, T. M. Rice, and M. Troyer, Competing States in the $t - J$ -Model: Uniform d -Wave State versus Stripe State, *Phys. Rev. Lett.* **113**, 046402 (2014).
- [10] Y.-C. He, M. P. Zaletel, M. Oshikawa, and F. Pollmann, Signatures of Dirac cones in a DMRG study of the kagome Heisenberg model, *Phys. Rev. X* **7**, 031020 (2017).
- [11] M. Gohlke, G. Wachtel, Y. Yamaji, F. Pollmann, and Y. B. Kim, Quantum spin liquid signatures in Kitaev-like frustrated magnets, *Phys. Rev. B* **97**, 075126 (2018).
- [12] F. Pollmann, A. M. Turner, E. Berg, and M. Oshikawa, Entanglement spectrum of a topological phase in one dimension, *Phys. Rev. B* **81**, 064439 (2010).
- [13] N. Schuch, D. Pérez-García, and I. Cirac, Classifying quantum phases using matrix product states and projected entangled pair states, *Phys. Rev. B* **84**, 165139 (2011).
- [14] D. J. Williamson, N. Bultinck, M. Mariën, M. B. Şahinoğlu, J. Haegeman, and F. Verstraete, Matrix product operators for symmetry-protected topological phases: Gauging and edge theories, *Phys. Rev. B* **94**, 205150 (2016).

- (2016).
- [15] T. B. Wahl, Tensor networks demonstrate the robustness of localization and symmetry-protected topological phases, *Phys. Rev. B* **98**, 054204 (2018).
- [16] A. Chan and T. B. Wahl, Classification of symmetry-protected topological many-body localized phases in one dimension, *J. Phys. Cond. Mat.* **32**, 305601 (2020).
- [17] J. Li, A. Chan, and T. B. Wahl, Classification of symmetry-protected topological phases in two-dimensional many-body localized systems, *Phys. Rev. B* **102**, 014205 (2020).
- [18] X.-L. Qi and S.-C. Zhang, Topological insulators and superconductors, *Rev. Mod. Phys.* **83**, 1057 (2011).
- [19] M. Z. Hasan and C. L. Kane, Colloquium, *Rev. Mod. Phys.* **82**, 3045 (2010).
- [20] L. Fu, Topological Crystalline Insulators, *Phys. Rev. Lett.* **106**, 106802 (2011).
- [21] R.-J. Slager, A. Mesáros, V. Juričić, and J. Zaane, The space group classification of topological band-insulators, *Nat. Phys.* **9**, 98 (2013).
- [22] H. C. Po, A. Vishwanath, and H. Watanabe, Symmetry-based indicators of band topology in the 230 space groups, *Nat. Commun.* **8**, 50 (2017).
- [23] B. Bradlyn, L. Elcoro, J. Cano, M. G. Vergniory, Z. Wang, C. Felser, M. I. Aroyo, and B. A. Bernevig, Topological quantum chemistry, *Nature* **547**, 298 (2017).
- [24] R.-J. Slager, The translational side of topological band insulators, *J. Phys. Chem. Solids* **128**, 24 (2019).
- [25] A. Bouhon, T. Bzdušek, and R.-J. Slager, Geometric approach to fragile topology beyond symmetry indicators, *Phys. Rev. B* **102**, 115135 (2020).
- [26] K. Shiozaki and M. Sato, Topology of crystalline insulators and superconductors, *Phys. Rev. B* **90**, 165114 (2014).
- [27] J. Dubail and N. Read, Tensor network trial states for chiral topological phases in two dimensions and a no-go theorem in any dimension, *Phys. Rev. B* **92**, 205307 (2015).
- [28] T. B. Wahl, H.-H. Tu, N. Schuch, and J. I. Cirac, Projected Entangled-Pair States Can Describe Chiral Topological States, *Phys. Rev. Lett.* **111**, 236805 (2013).
- [29] S. Yang, T. B. Wahl, H.-H. Tu, N. Schuch, and J. I. Cirac, Chiral Projected Entangled-Pair State with Topological Order, *Phys. Rev. Lett.* **114**, 106803 (2015).
- [30] A. Kitaev, Periodic table for topological insulators and superconductors, *AIP Conf. Proc.* **1134**, 22 (2009).
- [31] N. Read, Compactly supported Wannier functions and algebraic K -theory, *Phys. Rev. B* **95**, 115309 (2017).
- [32] P. Törmä, Essay: Where Can Quantum Geometry Lead Us?, *Phys. Rev. Lett.* **131**, 240001 (2023).
- [33] A. Bouhon, A. Timmel, and R.-J. Slager, Quantum geometry beyond projective single bands (2023), [arXiv:2303.02180](https://arxiv.org/abs/2303.02180).
- [34] J. Provost and G. Vallee, Riemannian structure on manifolds of quantum states, *Commun. Math. Phys.* **76**, 289 (1980).
- [35] R. Resta, The insulating state of matter: a geometrical theory, *Euro. Phys. Jour. B* **79**, 121 (2011).
- [36] F. Verstraete and J. I. Cirac, Renormalization algorithms for quantum-many body systems in two and higher dimensions, [arXiv:cond-mat/0407066](https://arxiv.org/abs/cond-mat/0407066) (2004).
- [37] A. Bouhon, Q. Wu, R.-J. Slager, H. Weng, O. V. Yazyev, and T. Bzdušek, Non-Abelian reciprocal braiding of Weyl points and its manifestation in ZrTe, *Nat. Phys.* **16**, 1137 (2020).
- [38] J. Ahn, S. Park, and B.-J. Yang, Failure of Nielsen-Ninomiya Theorem and Fragile Topology in Two-Dimensional Systems with Space-Time Inversion Symmetry: Application to Twisted Bilayer Graphene at Magic Angle, *Phys. Rev. X* **9**, 021013 (2019).
- [39] A. Bouhon, A. M. Black-Schaffer, and R.-J. Slager, Wilson loop approach to fragile topology of split elementary band representations and topological crystalline insulators with time-reversal symmetry, *Phys. Rev. B* **100**, 195135 (2019).
- [40] Q. Wu, A. A. Soluyanov, and T. Bzdušek, Non-Abelian band topology in noninteracting metals, *Science* **365**, 1273 (2019).
- [41] R.-J. Slager, A. Bouhon, and F. N. Ünal, Non-Abelian Floquet braiding and anomalous Dirac string phase in periodically driven systems, *Nat Commun* **15**, 1144 (2024).
- [42] F. N. Ünal, A. Bouhon, and R.-J. Slager, Topological Euler Class as a Dynamical Observable in Optical Lattices, *Phys. Rev. Lett.* **125**, 053601 (2020).
- [43] W. Zhao, Y.-B. Yang, Y. Jiang, Z. Mao, W. Guo, L. Qiu, G. Wang, L. Yao, L. He, Z. Zhou, Y. Xu, and L. Duan, Quantum simulation for topological Euler insulators, *Commun. Phys.* **5**, 223 (2022).
- [44] B. Peng, A. Bouhon, B. Monserrat, and R.-J. Slager, Phonons as a platform for non-Abelian braiding and its manifestation in layered silicates, *Nat. Commun.* **13**, 423 (2022).
- [45] B. Peng, A. Bouhon, R.-J. Slager, and B. Monserrat, Multigap topology and non-Abelian braiding of phonons from first principles, *Phys. Rev. B* **105**, 085115 (2022).
- [46] A. Bouhon, G. F. Lange, and R.-J. Slager, Topological correspondence between magnetic space group representations and subdimensions, *Phys. Rev. B* **103**, 245127 (2021).
- [47] S. H. Lee, Y. Qian, and B.-J. Yang, Euler band topology in spin-orbit coupled magnetic systems, [arXiv:2404.16383](https://arxiv.org/abs/2404.16383) (2024).
- [48] B. Jiang, A. Bouhon, Z.-K. Lin, X. Zhou, B. Hou, F. Li, R.-J. Slager, and J.-H. Jiang, Experimental observation of non-Abelian topological acoustic semimetals and their phase transitions, *Nat. Phys.* **17**, 1239 (2021).
- [49] B. Jiang, A. Bouhon, S.-Q. Wu, Z.-L. Kong, Z.-K. Lin, R.-J. Slager, and J.-H. Jiang, Observation of an acoustic topological Euler insulator with meronic waves, *Science Bulletin* **69**, 1653 (2024).
- [50] Q. Guo, T. Jiang, R.-Y. Zhang, L. Zhang, Z.-Q. Zhang, B. Yang, S. Zhang, and C. T. Chan, Experimental observation of non-Abelian topological charges and edge states, *Nature* **594**, 195 (2021).
- [51] A. Y. Kitaev, Unpaired Majorana fermions in quantum wires, *Physics-Uspekhi* **44**, 131 (2001).
- [52] Z. Xie, J. Chen, J. Yu, X. Kong, B. Normand, and T. Xiang, Tensor Renormalization of Quantum Many-Body Systems Using Projected Entangled Simplex States, *Phys. Rev. X* **4**, 011025 (2014).
- [53] T. B. Wahl, S. T. Haßler, H.-H. Tu, J. I. Cirac, and N. Schuch, Symmetries and boundary theories for chiral projected entangled pair states, *Phys. Rev. B* **90**, 115133 (2014).
- [54] W. Dür, G. Vidal, and J. I. Cirac, Three qubits can be entangled in two inequivalent ways, *Phys. Rev. A* **62**, 062314 (2000).

- [55] S. Kwon and B.-J. Yang, Quantum geometric bound and ideal condition for Euler band topology, *Phys. Rev. B* **109**, L161111 (2024).
- [56] See Supplemental Material at [url] for the momentum-space characterization in the non-interacting limit, quantum-geometrical features, the non-interacting entanglement spectrum, and quantum Fisher information and the quantum Cramer-Rao bound of the ideal Euler bands..
- [57] S. L. Braunstein and C. M. Caves, Statistical distance and the geometry of quantum states, *Phys. Rev. Lett.* **72**, 3439 (1994).
- [58] J. Liu, H. Yuan, X.-M. Lu, and X. Wang, Quantum Fisher information matrix and multiparameter estimation, *J. Phys. A: Math. Theor.* **53**, 023001 (2019).
- [59] B. Mera, A. Zhang, and N. Goldman, Relating the topology of Dirac Hamiltonians to quantum geometry: When the quantum metric dictates Chern numbers and winding numbers, *SciPost Phys.* **12**, 018 (2022).
- [60] M. Yu, X. Li, Y. Chu, B. Mera, F. N. Ünal, P. Yang, Y. Liu, N. Goldman, and J. Cai, Experimental demonstration of topological bounds in quantum metrology, *Nat. Sci. Rev.* , nwae065 (2024).
- [61] J. Hauschild and F. Pollmann, Efficient numerical simulations with Tensor Networks: Tensor Network Python (TeNPy), *SciPost Phys. Lect. Notes* , 5 (2018), code available from <https://github.com/tenpy/tenpy>.
- [62] A. Bouhon and R.-J. Slager, Multi-gap topological conversion of Euler class via band-node braiding: minimal models, *PT*-linked nodal rings, and chiral heirs, [arXiv:2203.16741](https://arxiv.org/abs/2203.16741) (2022).
- [63] W. J. Jankowski, A. S. Morris, A. Bouhon, F. N. Ünal, and R.-J. Slager, Optical manifestations of topological Euler class in electronic materials, [arXiv:2311.07545](https://arxiv.org/abs/2311.07545) (2023).
- [64] Q. Niu, D. J. Thouless, and Y.-S. Wu, Quantized Hall conductance as a topological invariant, *Phys. Rev. B* **31**, 3372 (1985).
- [65] I. Peschel, Calculation of reduced density matrices from correlation functions, *J. Phys. A Math. Gen.* **36**, L205 (2003).
- [66] R. Takahashi and T. Ozawa, Bulk-edge correspondence of Stiefel-Whitney and Euler insulators through the entanglement spectrum and cutting procedure, *Phys. Rev. B* **108**, 075129 (2023).

Momentum-space characterization of the model in the non-interacting limit

We demonstrate how the model introduced in the main text, Eq. (2), can be decomposed in momentum space. We first Fourier transform the real-space creation and annihilation operators to the basis of Bloch orbitals: $a_{\alpha,\mathbf{k}}^{(\dagger)} = \frac{1}{\sqrt{N}} \sum_{\mathbf{R}_i} e^{(\pm)i\mathbf{k}\cdot(\mathbf{R}_i+\mathbf{r}_\alpha)} a_{\alpha,i}^{(\dagger)}$. Here, the operator $a_{\alpha,i}^{(\dagger)}$ creates/annihilates a single particle in an atomic orbital $\alpha = A, B, C$ situated at the position \mathbf{r}_α with respect to the position vector of a unit cell center \mathbf{R}_i , where $i = 1, \dots, N$. Under the translational symmetry, one obtains:

$$H = \sum_{\mathbf{k}; \alpha, \beta = A, B, C} H_{\alpha\beta}(\mathbf{k}) a_{\alpha,\mathbf{k}}^\dagger a_{\beta,\mathbf{k}}. \quad (13)$$

Here, the Bloch Hamiltonian for the considered system on the kagome lattice, manifestly expressed in a real gauge, reads [48, 49]:

$$H(\mathbf{k}) = \begin{pmatrix} H_{AA}(\mathbf{k}) & H_{AB}(\mathbf{k}) & H_{AC}(\mathbf{k}) \\ H_{AB}(\mathbf{k}) & H_{BB}(\mathbf{k}) & H_{BC}(\mathbf{k}) \\ H_{AC}(\mathbf{k}) & H_{BC}(\mathbf{k}) & H_{CC}(\mathbf{k}) \end{pmatrix}, \quad (14)$$

with the corresponding (real) matrix elements, on setting $t = t' = t'' = -1$,

$$H_{AA}(\mathbf{k}) = -\mu + 2 \cos(k_1), \quad (15)$$

$$H_{AB}(\mathbf{k}) = 2 \cos(k_1/2 + k_2/2) + 2 \cos(k_1/2 - k_2/2), \quad (16)$$

$$H_{AC}(\mathbf{k}) = 2 \cos(k_2/2) + 2 \cos(k_1 + k_2/2), \quad (17)$$

$$H_{BB}(\mathbf{k}) = -\mu + 2 \cos(k_2), \quad (18)$$

$$H_{BC}(\mathbf{k}) = 2 \cos(k_1/2) + 2 \cos(k_1/2 + k_2), \quad (19)$$

$$H_{CC}(\mathbf{k}) = -\mu + 2 \cos(k_1 + k_2). \quad (20)$$

We recognize that the Bloch Hamiltonian can be further rewritten as,

$$H(\mathbf{k}) = \begin{pmatrix} -\mu - 2 + 4 \cos^2(k_1/2) & 4 \cos(k_1/2) \cos(k_2/2) & 4 \cos(k_1/2) \cos(k_1/2 + k_2/2) \\ 4 \cos(k_1/2) \cos(k_2/2) & -\mu - 2 + 4 \cos^2(k_2/2) & 4 \cos(k_2/2) \cos(k_1/2 + k_2/2) \\ 4 \cos(k_1/2) \cos(k_1/2 + k_2/2) & 4 \cos(k_2/2) \cos(k_1/2 + k_2/2) & -\mu - 2 + 4 \cos^2(k_1/2 + k_2/2) \end{pmatrix}, \quad (21)$$

or more compactly,

$$H(\mathbf{k}) = (-\mu - 2)\mathbb{1}_3 + 4\mathbf{n}(\mathbf{k}) \otimes \mathbf{n}(\mathbf{k})^T, \quad (22)$$

with $\mathbf{n}(\mathbf{k}) = \left(\cos(k_1/2), \cos(k_2/2), \cos(k_1/2 + k_2/2) \right)^T$. Importantly, under such decomposition, the topology of the Euler bands in any three-band Hamiltonian satisfying a reality condition [$H(\mathbf{k}) = H^*(\mathbf{k})$] can be captured by the normalized vector $\hat{\mathbf{n}}(\mathbf{k}) = \mathbf{n}(\mathbf{k})/\|\mathbf{n}(\mathbf{k})\|$. In particular, in the considered model, the vector $\hat{\mathbf{n}}(\mathbf{k})$ reads

$$\hat{\mathbf{n}}(\mathbf{k}) = \frac{1}{\sqrt{\cos^2(k_1/2) + \cos^2(k_2/2) + \cos^2(k_1/2 + k_2/2)}} \begin{pmatrix} \cos(k_1/2) \\ \cos(k_2/2) \\ \cos(k_1/2 + k_2/2) \end{pmatrix}, \quad (23)$$

and it fully determines the Euler curvature as

$$\text{Eu} = \hat{\mathbf{n}} \cdot (\partial_{k_2} \hat{\mathbf{n}} \times \partial_{k_1} \hat{\mathbf{n}}). \quad (24)$$

The Euler curvature can be viewed as a skyrmion density in the momentum-space texture, with the skyrmion being spanned by $\hat{\mathbf{n}}$ over the Brillouin zone (BZ) square/torus. In particular, the Euler invariant is given by [37, 48]

$$\chi = \frac{1}{2\pi} \int_{\text{BZ}} d^2\mathbf{k} \text{Eu} = \frac{1}{2\pi} \int_{\text{BZ}} d^2\mathbf{k} \hat{\mathbf{n}} \cdot (\partial_{k_2} \hat{\mathbf{n}} \times \partial_{k_1} \hat{\mathbf{n}}) = 2Q, \quad (25)$$

and obtains $\chi = 1$ in the case of interest, which corresponds to the momentum-space meron (half-skyrmion) with the half-skyrmion number $Q = 1/2$ [49]. Additionally, the vector $\mathbf{n}(\mathbf{k})$ fully captures the band dispersion present in the model, as Eq. (22) can be written as,

$$H(\mathbf{k}) = (-\mu - 2)\mathbb{1}_3 + 4\|\mathbf{n}(\mathbf{k})\|^2 \hat{\mathbf{n}}(\mathbf{k}) \otimes \hat{\mathbf{n}}(\mathbf{k})^T, \quad (26)$$

explicitly determining the band dispersion in the third band as $E_3(\mathbf{k}) = (-\mu - 2) + 4\|\mathbf{n}(\mathbf{k})\|^2$, contrary to the flat-band dispersion in the bottom Euler bands $E_1(\mathbf{k}) = E_2(\mathbf{k}) = (-\mu - 2)$. The band energies given by such dispersions manifestly have a gap across the entire Brillouin zone, as the norm of the vector $\mathbf{n}(\mathbf{k})$ is non-vanishing $\|\mathbf{n}(\mathbf{k})\| > 0$ at every \mathbf{k} -point. This follows from the fact that the components of the vector $\mathbf{n}(\mathbf{k})$, $\cos(k_1/2)$, $\cos(k_2/2)$, $\cos(k_1/2 + k_2/2)$ are not independent, with at least one of those terms being necessarily non-vanishing at any \mathbf{k} -point.

Quantum geometry in the free fermion limit

Here, we elaborate on the quantum geometry of the model in non-interacting limit. Consistently with the Plücker formalism for multi-band quantum geometry introduced in Ref. [33], we first define the Fubini-Study metric ($ds^2 = 1 - |\langle u_1(\mathbf{k}) \wedge \dots \wedge u_n(\mathbf{k}) | u_1(\mathbf{k} + d\mathbf{k}) \wedge \dots \wedge u_n(\mathbf{k} + d\mathbf{k}) \rangle|^2$) in the set of occupied Bloch bands $\{|u_n(\mathbf{k})\}$ [34],

$$ds^2 = g_{ij}^\chi(\mathbf{k}) dk_i dk_j \quad (27)$$

where g_{ij}^χ is the quantum metric in the Euler flat bands, and the Einstein summation convention was assumed. With both of the Euler bands $n = 1, 2$ occupied ('occ'), we can correspondingly write the metric as

$$g_{ij}^\chi(\mathbf{k}) = \sum_n^{\text{occ}} \frac{1}{2} \left[\langle \partial_{k_i} u_n(\mathbf{k}) | \hat{Q} | \partial_{k_j} u_n(\mathbf{k}) \rangle + \text{c.c.} \right] = \langle \partial_{k_i} u_1(\mathbf{k}) | u_3(\mathbf{k}) \rangle \langle u_3(\mathbf{k}) | \partial_{k_j} u_1(\mathbf{k}) \rangle + \langle \partial_{k_i} u_2(\mathbf{k}) | u_3(\mathbf{k}) \rangle \langle u_3(\mathbf{k}) | \partial_{k_j} u_2(\mathbf{k}) \rangle, \quad (28)$$

where $\hat{Q} = \sum_m^{\text{unocc}} |u_m(\mathbf{k})\rangle \langle u_m(\mathbf{k})| = |u_3(\mathbf{k})\rangle \langle u_3(\mathbf{k})|$ is the projector onto unoccupied ('unocc') band(s); here, $m = 3$. In the second equality, we used the fact that the eigenvectors representing the Euler bands are chosen real, as here, the Bloch Hamiltonian $H(\mathbf{k}) = \sum_{i=1}^3 E_i(\mathbf{k}) |u_i(\mathbf{k})\rangle \langle u_i(\mathbf{k})|$ is a real symmetric matrix. The quantum metric is manifestly real and symmetric, by definition Eq. (28).

Alternatively, we can rewrite the metric in terms of the projector onto the unoccupied band as,

$$\begin{aligned} g_{ij}^\chi &= \text{Tr}_{\text{occ}}[(\partial_{k_i} \hat{Q})(\partial_{k_j} \hat{Q})] = \text{Tr}_{\text{occ}}(|\partial_{k_i} u_3(\mathbf{k})\rangle \langle \partial_{k_j} u_3(\mathbf{k})| + |u_3(\mathbf{k})\rangle \langle u_3(\mathbf{k})| \partial_{k_i} u_3(\mathbf{k}) \langle \partial_{k_j} u_3(\mathbf{k})| \\ &\quad + |u_3(\mathbf{k})\rangle \langle \partial_{k_i} u_3(\mathbf{k})| u_3(\mathbf{k}) \langle \partial_{k_j} u_3(\mathbf{k})| + |u_3(\mathbf{k})\rangle \langle \partial_{k_i} u_3(\mathbf{k})| \partial_{k_j} u_3(\mathbf{k}) \langle u_3(\mathbf{k})|) \\ &= \langle \partial_{k_i} u_3(\mathbf{k}) | \partial_{k_j} u_3(\mathbf{k}) \rangle - \langle \partial_{k_i} u_3(\mathbf{k}) | u_3(\mathbf{k}) \rangle \langle u_3(\mathbf{k}) | \partial_{k_j} u_3(\mathbf{k}) \rangle = \langle \partial_{k_i} u_3(\mathbf{k}) | \partial_{k_j} u_3(\mathbf{k}) \rangle \end{aligned} \quad (29)$$

where the last equality follows from the reality condition. We now use the fact that the third Bloch band defines a normalized vector field: $\hat{\mathbf{n}}(\mathbf{k}) \hat{=} |u_3(\mathbf{k})\rangle$, as follows from the spectral decomposition of the Hamiltonian.

In terms of the momentum-space vector $\hat{\mathbf{n}}$, the quantum metric in a three-band Euler Hamiltonian reads [63]

$$g_{ij}^x = (\partial_{k_i} \hat{\mathbf{n}}) \cdot (\partial_{k_j} \hat{\mathbf{n}}), \quad (30)$$

which obtains an inequality [55],

$$\sqrt{\det \mathbf{g}^x} \geq |\text{Eu}|. \quad (31)$$

Additionally, from inequality between arithmetic and geometric means, we directly obtain,

$$\text{Tr} \mathbf{g}^x \equiv g_{11}^x + g_{22}^x \geq 2\sqrt{g_{11}^x g_{22}^x} \geq 2\sqrt{g_{11}^x g_{22}^x - (g_{12}^x)^2} \equiv 2\sqrt{\det \mathbf{g}^x} \geq 2|\text{Eu}|, \quad (32)$$

where we used the symmetry of the (real) metric tensor $g_{12}^x = g_{21}^x$.

In the considered model, the metric elements read:

$$g_{11}^x = \frac{8 - 3 \cos k_1 - 3 \cos(k_1 + k_2) - \cos(k_1 - k_2) - \cos(k_1 + 2k_2)}{8(3 + \cos k_1 + \cos k_2 + \cos(k_1 + k_2))^2}, \quad (33)$$

$$g_{22}^x = \frac{8 - 3 \cos k_2 - 3 \cos(k_1 + k_2) - \cos(k_1 - k_2) - \cos(2k_1 + k_2)}{8(3 + \cos k_1 + \cos k_2 + \cos(k_1 + k_2))^2}, \quad (34)$$

$$g_{12}^x = g_{21}^x = \frac{2 - 2 \cos k_1 \cos k_2 + \sin k_1 \sin k_2}{4(3 + \cos k_1 + \cos k_2 + \cos(k_1 + k_2))^2}, \quad (35)$$

which directly obtains the quantum volume [55],

$$\sqrt{\det \mathbf{g}^x(\mathbf{k})} = \frac{-3 + \cos k_1 + \cos k_2 + \cos(k_1 + k_2)}{4\sqrt{2}(3 + \cos k_1 + \cos k_2 + \cos(k_1 + k_2))^{3/2}}, \quad (36)$$

as well as

$$\text{Tr} \mathbf{g}^x(\mathbf{k}) = \frac{16 - 3 \cos k_1 - 3 \cos k_2 - 6 \cos(k_1 + k_2) - 2 \cos(k_1 - k_2) - \cos(2k_1 + k_2) - \cos(k_1 + 2k_2)}{8(3 + \cos k_1 + \cos k_2 + \cos(k_1 + k_2))^2}. \quad (37)$$

On the contrary, the Euler curvature in the model is given by the following expression

$$\text{Eu}(\mathbf{k}) = \frac{-3 + \cos k_1 + \cos k_2 + \cos(k_1 + k_2)}{4\sqrt{2}(3 + \cos k_1 + \cos k_2 + \cos(k_1 + k_2))^{3/2}}. \quad (38)$$

We note that, analytically, an inequality $\text{Tr} \mathbf{g}^x(\mathbf{k}) \geq 2|\text{Eu}(\mathbf{k})|$ holds, on substituting the individual quantum metric matrix elements to the bound between the determinant and trace. The equality of the determinant (quantum volume) and the Euler curvature follows trivially by inspection, as the analytical expressions for both quantities are identical across the entire momentum space.

Moreover, beyond the single-particle context, we can consider many-body quantum metric $g_{ij}(\theta)$ defined in terms of the twist angles $\theta = (\theta_1, \theta_2)$ and the twisted boundary conditions [64],

$$\psi(\{x_i + L_1\}, \{y_i\}) \equiv \langle \{x_i + L_1\}, \{y_i\} | \psi \rangle = e^{i\theta_1} \psi(\{x_i\}, \{y_i\}), \quad (39)$$

$$\psi(\{x_i\}, \{y_i + L_2\}) \equiv \langle \{x_i\}, \{y_i + L_2\} | \psi \rangle = e^{i\theta_2} \psi(\{x_i\}, \{y_i\}), \quad (40)$$

where $i = 1, 2, \dots, N_{\text{tot}}$ are particle labels, x_i and y_i the sets of coordinates of fermions i , and L_1, L_2 denote the cell lengthscales, on which the twisted periodic boundary conditions were imposed on the many-body state.

In terms of the twist angles, the many-body quantum metric reads

$$g_{ij}(\theta) = \Re \langle \partial_{\theta_i} \psi(\theta) | (1 - \hat{P}_\theta) | \partial_{\theta_j} \psi(\theta) \rangle, \quad (41)$$

with the projector onto the many-body ground state $\hat{P}_\theta = |\psi(\theta)\rangle\langle\psi(\theta)|$. At the zero twist angle $\theta = (0, 0) \equiv \mathbf{0}$, in the free-fermion limit, we retrieve a many-body bound,

$$g_{ij}(\mathbf{0}) = \frac{1}{L_1 L_2} \sum_{\mathbf{k}} \text{Tr} \mathbf{g}^x(\mathbf{k}) \geq \frac{4\pi A}{L_1 L_2} |\chi|, \quad (42)$$

where A is the area of the unit cell of the system. However, we note that unlike in the case of the determinant bound providing an ideal condition on Euler bands, this many-body bound does not saturate in the considered models, as it reduces to the trace bound in the free particle limit. In other words, here, the strong inequalities rather than equalities hold within the proposed models.

Entanglement spectra of the non-interacting PEPS

Here we present the entanglement spectrum of the non-interacting kagome Euler model of the main text. For this purpose, we start with the momentum space Hamiltonian defined on a thin torus, *i.e.*, $L_x \gg L_y$. In the insulating state, the bottom two flat bands are occupied and the dispersive conduction band is empty. We first write down the projector on the occupied state

$$\hat{P}(\mathbf{k}) = \sum_{i \in \text{occupied}} |\psi_i(\mathbf{k})\rangle\langle\psi_i(\mathbf{k})|. \quad (43)$$

The projector by definition has its eigenvalues restricted to 0 and 1. For the calculations performed on a lattice, we define the real space positions as $\mathbf{r} = n_1 \mathbf{a}_1 + n_2 \mathbf{a}_2$, where $n_{1(2)} \in \mathbb{Z}$ and $\mathbf{a}_{1(2)}$ are the lattice vectors. The corresponding reciprocal space momenta take the values as $\mathbf{k} = \frac{k_1}{2\pi} \mathbf{b}_1 + \frac{k_2}{2\pi} \mathbf{b}_2$, where $k_1, k_2 \in (-\pi, \pi]$ and $\mathbf{b}_{1(2)}$ are the reciprocal lattice vectors. For the kagome model here, we have chosen, $\mathbf{a}_1 = (\sqrt{3}/2, 1/2)$ and $\mathbf{a}_2 = (0, 1)$ as the lattice vectors. The corresponding reciprocal lattice vectors are $\mathbf{b}_1 = (4\pi/\sqrt{3}, 0)$ and $\mathbf{b}_2 = (-2\pi/\sqrt{3}, 2\pi)$. From the projector, we obtain a one-body correlation operator

$$G_{nm}(k_2) = \frac{1}{L_x} \sum_{k_1} \mathbf{e}^{i2\pi k_1(n-m)} \hat{P}(k_1, k_2). \quad (44)$$

Since G is also a projector, its eigenvalues are also restricted to 0 and 1. We partition the system into subsystems A and B, such that the entanglement spectrum between the two subsystems is given by the eigenvalues of the reduced density matrix ρ_A . The spectrum of the reduced density matrix ρ_A can then be obtained from the spectrum of the reduced correlation matrix G^A defined as [65]

$$G_{nm}^A(k_2) = G_{nm}(k_2); \quad n, m \in [0, L_1/2). \quad (45)$$

In Fig. 5 (a) and (c), we show the spectrum of the reduced one-body correlation matrix G^A . The plots are obtained for system sizes $L_x = 120$ and $L_y = 6$ (12) for (a) and (c) respectively. The eigenvalues $\Lambda_i(k_2)$ of G^A are bounded to lie in $[0, 1]$, although, unlike the projector eigenvalues, they are not restricted to be 0 and 1. Indeed the in-gap eigenvalues are related to the topological Euler class of the model [66]. However, unlike the well-known case of Chern insulators, these in-gap modes in the one-body correlation spectrum of the Euler topology are not related to the physical edge states due to non-trivial topology, which typically has a spectral flow between the bulk conduction and valence bands. In Fig. 5 (e) we explicitly show the absence of such topological edge states with a spectral flow between flat valence bands at -1 and dispersive conduction band. The physical energy spectrum is calculated for system size $L_1 = 120$ and $L_2 = 12$ with open boundary conditions along L_1 and periodic boundary conditions along L_2 .

From the spectrum of G^A , we obtain the entanglement spectrum of the non-interacting model using the relation

$$\varepsilon(k_2) = - \sum_{i \in \text{occupied}} \log[\Lambda_i(k_2)] - \sum_{j \in \text{unoccupied}} \log[1 - \Lambda_j(k_2)]. \quad (46)$$

To calculate the full many-body entanglement spectrum as shown in the figure, we first obtain the ground state of subsection A by occupying $2/3$ of the *highest* eigenvalues Λ_i , which is commensurate with the $2/3$ filling of the whole system. Here, one should keep in mind that since the projector P eigenvalues of the occupied states lie at 1 and unoccupied states at 0, while constructing the ground state of G^A , one should start counting from $\Lambda_i \rightarrow 1$ as

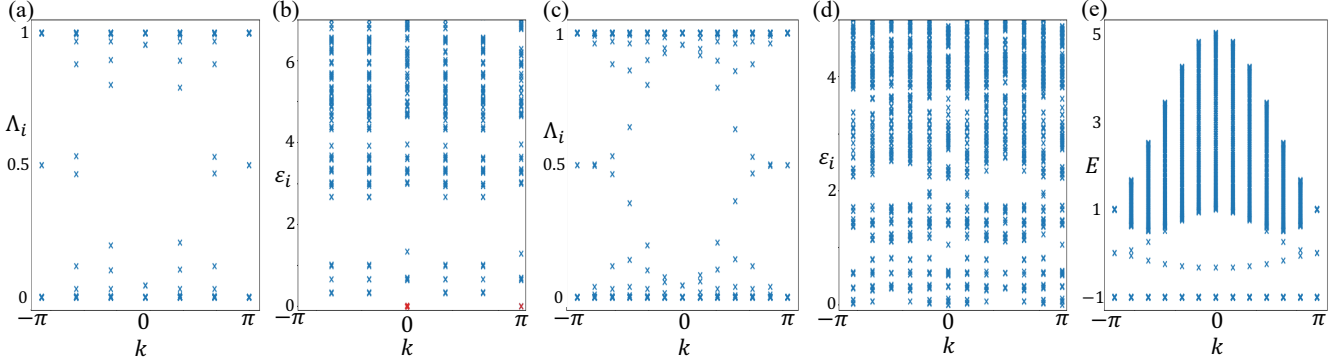


FIG. 5. Entanglement, one-body correlation, and physical spectra: (a) One-body correlation spectrum on a thin torus with $L_y = 6$, (b) Many-body entanglement spectrum on $L_y = 6$ torus. The red marker at $k = 0$ and $\epsilon_i = 0$ is the ground state of the partition 'A'. (c) and (d) are the one-body correlation spectrum and many-body entanglement spectrum for $L_y = 12$, respectively, to clarify the variation along k . (e) The physical spectrum on a cylinder of size $L_x = 120$ and $L_y = 12$ does not show an edge state with a spectral flow between the flat valence bands and dispersive conduction band.

occupied, and going down in the eigenvalues Λ_i corresponds to going up in the excitation spectrum. Once the ground state is identified, we obtain a many-body entanglement spectrum by creating excitations on this ground state. Since for the entanglement spectrum, we partition the system, while the filling fraction $2/3$ is a constraint for the whole system, the subsystem A has eigenstates that have particle numbers different to $2/3$ filling of the subsystem itself. Therefore to calculate the full many-body ground state, we first partition the subsystem A into different total particle number channels and from there create all possible particle-hole excitations. Then for each excited state configuration described by a fixed fermionic occupation number, we can obtain the entanglement spectrum using Eq. 46.

The many-body entanglement spectrum of the non-interacting model is shown in Fig. 5 (b) and (d) for the system size $L_x = 120$ and $L_y = 6(12)$ respectively. We have taken the ground state entanglement energy to zero as a reference, which is shown by the red marker at $k = 0$ in Fig. 5 (b) and (d). Notice the presence of the zero entanglement energy state at $k = \pi$. This is obtained by considering a channel with one less (or more) particle in subsystem A than the exact $2/3$ filling.

Comparing the many-body entanglement spectrum to the interacting case with $\alpha = 0$ in the main text (left panel in Fig. 4), we see a good agreement in their low energy features. In particular, in both cases, the ground state corresponds to $k = 0$ with the lowest entanglement energy. As we move to a finite k , the entanglement energy increases and eventually comes back down to the ground state value at $k = \pi$ creating a cusp-like feature in the low-energy entanglement spectrum. This low energy behavior can be traced back to the in-gap modes (around $\Lambda = 0.5$) in the one-body correlation spectrum shown in Fig. 5 (a) and (c). In one-body correlation spectrum, for each mode near 0, there are two modes near 1, and therefore $2/3$ filling corresponds to occupying all modes in the upper half of the correlation spectrum. The low energy excitations are then created near $\Lambda_i = 0.5$ with a very low energy cost, which leads to many low energy modes in the entanglement spectrum.

Quantum Fisher information and quantum Cramer-Rao bound of the ideal Euler bands

We further comment on the structures present in the models and their relation to quantum Fisher information (QFI) and the quantum Cramer-Rao (QCR) bound [57, 58]. Namely, we derive a non-Abelian QCR bound, which is induced by Euler topology and the Euler bands satisfying an ideal condition. The QCR bounds are of central relevance for quantum metrology [58].

To define the QFI in the context of this work, we consider a two-parameter family of single-particle states $|\psi_n(\mathbf{k})\rangle$, parametrized by $\mathbf{k} \equiv (k_1, k_2) \in T^2$, where T^2 denotes a two-torus. Consistently with the models introduced in the main text, at every point \mathbf{k} of the parameter space, we consider a three-state system. We take a spectral decomposition of the density matrix of the single-particle states at given \mathbf{k} -point, $\rho \equiv \sum_n \lambda_n |\psi_n(\mathbf{k})\rangle \langle \psi_n(\mathbf{k})|$. The QFI matrix for single-particle operators \hat{r}_1, \hat{r}_2 (conjugate to k_1, k_2), then reads [58],

$$F_{ij}[\rho] \equiv \sum_{m,n:\lambda_m+\lambda_n \geq 0} \frac{2(\lambda_m - \lambda_n)^2}{\lambda_m + \lambda_n} \langle \psi_m(\mathbf{k}) | \hat{r}_i | \psi_n(\mathbf{k}) \rangle \langle \psi_n(\mathbf{k}) | \hat{r}_j | \psi_m(\mathbf{k}) \rangle. \quad (47)$$

In translationally symmetric contexts, if the parameters \mathbf{k} were to be identified with momenta, then \hat{r}_1, \hat{r}_2 represent position operator components defined along the lattice vectors. We moreover recognize: $\hat{r}_i \sim i\partial_{k_i}$, i.e. $-i\partial_{k_i}\rho = [\rho, \hat{r}_i]$, and hence, $-i\langle\psi_m(\mathbf{k})|\partial_{k_i}\rho|\psi_n(\mathbf{k})\rangle = \langle\psi_m(\mathbf{k})|[\rho, \hat{r}_i]|\psi_n(\mathbf{k})\rangle = (\lambda_m - \lambda_n)\langle\psi_m(\mathbf{k})|\hat{r}_i|\psi_n(\mathbf{k})\rangle$. Therefore, for pure states, where in the context of this work we can consider single particle in the third band within the corresponding three-state problem, i.e. $\rho = |\psi_3(\mathbf{k})\rangle\langle\psi_3(\mathbf{k})| = |u_3(\mathbf{k})\rangle\langle u_3(\mathbf{k})|$; the QFI matrix reduces to the quantum metric (see the main text),

$$F_{ij}[\rho] = 4g_{ij}^X(\mathbf{k}). \quad (48)$$

The QCR bound [57, 58] for the two-parameter measurements can be captured by the covariance matrix Σ with [58, 60],

$$\Sigma(\hat{\mathbf{k}}) \geq \frac{1}{M}F^{-1}[\rho], \quad (49)$$

where M is the number of the repetitions of measurements [58–60]. The covariance matrix for an unbiased estimator $\hat{\mathbf{k}}$ for the two-parameter family $\mathbf{k} = (k_1, k_2)$ under a set of positive operator-valued measurements (POVM), Π_p , such that $\sum_p^{N_p} \Pi_p = 1$, $\Pi_p \Pi_{p'} = \Pi_p \delta_{pp'}$, with $N_p \geq 3$; is defined as [58, 59],

$$\Sigma_{ij}(\hat{\mathbf{k}}) = \langle\delta k_i \delta k_j\rangle \equiv \sum_p k_i k_j \text{Tr}[\rho \Pi_p] - k_i k_j, \quad (50)$$

where $\langle\dots\rangle \equiv \text{Tr}[\rho(\dots)]$. For ideal bands, as in the introduced model, the Euler curvature determines the quantum-metrological bound at every point of the parameter space as,

$$\sqrt{\det \Sigma(\hat{\mathbf{k}})} \geq \frac{1}{M\sqrt{\det \mathbf{g}^X(\mathbf{k})}} = \frac{1}{M|\text{Eu}(\mathbf{k})|}, \quad (51)$$

where the first inequality follows from the derivation of Ref. [59], and the second equality is realized in the models introduced in our work.

Beyond the demonstrated quantum-metrological manifestations, the realized ideal condition for the Euler bands opens avenues for exotic fractionalization of the excitations in the topological bands, and offers a platform for exploring further deeper connections to the many-body quantum metric under twisted boundary conditions.
